J. Electrochem. Sci. Eng. **16** (2026) 2951; http://doi.org/10.5599/jese.2951

Open Access : ISSN 1847-9286
https://pub.iapchem.org/ojs/index.php/JESE

Original scientific paper

$CoNb_2O_6$ embedded in graphene nanosheets as an advanced intercalation anode for high-energy lithium-ion capacitors

Yaohong Hai[1], Xu Zhang[1,2,✉], Fuyan Ma[1], Yuxuan Chen[1], Lixiong He[1], Shiyi Zhang[1], Chunping Hou[1,2], Zhongli Zou[1,2,✉] and Kui Cheng[3]

[1]*School of Materials Science and Engineering, North Minzu University, Yinchuan, 750021, China*
[2]*Ningxia Research Center of Silicon Target and Silicon-Carbon Negative Materials Engineering Technology, China*
[3]*College of Engineering, Northeast Agricultural University, Harbin, 150030, China*
Corresponding author: ✉*zhangxu1024@nmu.edu.cn;* Tel.: +86-188-9500-5977

Received: August 8, 2025; Accepted: November 3, 2025; Published: November 10, 2025

Abstract

Intercalation anode materials are promising candidates for hybrid lithium-ion capacitors (LICs) owing to their excellent lithium storage capacity and cycling stability. In this study, a composite of $CoNb_2O_6$ embedded in graphene nanosheets ($CoNb_2O_6$@G) was synthesized via a two-step hydrothermal method and demonstrated for the first time as an intercalation anode material for lithium storage. The graphene sheets form a three-dimensional porous framework that provides abundant binding sites for the $CoNb_2O_6$ particles, effectively mitigating particle agglomeration and volume expansion during charge-discharge cycles. The composite with the optimal graphene content of 100 mg ($CoNb_2O_6$@G-100mg) exhibited a remarkable reversible capacity of 508.5 mA h g^{-1} at a current density of 50 mA g^{-1}. Furthermore, the $CoNb_2O_6$@G-100mg//activated carbon (AC) LIC, in which $CoNb_2O_6$@G-100mg and AC are used as the anode and cathode, respectively, exhibited an energy density of 94.1 W h kg^{-1} and a maximum power density of 8750 W kg^{-1} within the voltage range of 0.0 to 3.5 V. The device demonstrated outstanding cycling stability, with negligible capacity loss (0.00255% per cycle) over 10,000 charge-discharge cycles. These results demonstrate the potential of $CoNb_2O_6$@G as a high-performance anode material for energy-storage devices, particularly in power-oriented applications.

Keywords

Binary metal niobium oxides; long cycle life; high energy density; lithium storage

Introduction

Power supply systems are facing increasingly stringent requirements for long-term cycle stability and high power and energy densities owing to the rapid development and increasing popularity of hybrid electric vehicles (HEVs). Lithium-ion batteries, which store energy *via* insertion and removal of lithium ions between the anode and cathode, offer high energy densities ranging from

150 to 200 Wh kg^{-1}, but relatively low power density (<1000 W kg^{-1}) owing to their sluggish electrode kinetics. In contrast, supercapacitors exhibit high power densities (>10 kW kg^{-1}) and ultra-long lifespans (>10000 cycles) because of their rapid ion adsorption/desorption or surface redox reactions. Nonetheless, their utility is limited owing to their low energy density (<10 Wh kg^{-1}) [1-3]. Accordingly, neither supercapacitors nor lithium-ion batteries alone can fully satisfy the requirements of power-dense devices, while the combination of these technologies increases the size and cost of the power supply, which is unsuitable for the lightweight and compact designs of modern devices.

Lithium-ion capacitors (LICs) offer a promising solution to the challenges faced by high-performance energy-storage devices. Asymmetric LICs combine the lithium-ion insertion/removal of lithium-ion batteries with the rapid ion adsorption/desorption of electric double-layer capacitors, resulting in a high power/energy density, and long cycle life (compared to supercapacitors) without sacrificing the overall performance. LICs are therefore considered ideal power sources for high-power electronic devices, including HEVs.

The efficacy of LICs is determined by the strategic combination of anode and cathode materials, which aims to minimize disparities in reaction kinetics and enhance the overall device performance. In parallel, the operational characteristics of batteries are shaped by the electrodes' energy storage capabilities, as well as the rates of ion diffusion and the kinetics of electrochemical reactions during charging and discharging cycles. Consequently, selecting suitable electrode materials is essential for achieving optimal power density, energy density, and long-term cycling durability in LICs. Contemporary anode materials for LICs encompass those based on intercalation, conversion, and alloying mechanisms. Intercalation-type materials, such as titanium-based oxides [4] and carbon-based materials, store energy through reversible ion insertion into the host lattice, accompanied by redox reactions, thereby avoiding phase transitions and maintaining structural stability. This mechanism ensures minimal volume variation, excellent cycling reversibility, and rapid ion diffusion kinetics. In contrast, the electrochemical reactions of conversion-type materials (*e.g.* Fe_2O_3 [5] and Si) involve complete bond cleavage and reconstruction, whereas alloy-type materials such as Sn and Ni [6] operate *via* ion alloying mechanisms. Despite their high theoretical specific capacities, conversion- and alloy-type materials exhibit substantial volume fluctuations during cycling, causing irreversible electrode damage and accelerated capacity degradation. Intercalation-type materials are therefore more suitable for practical LIC applications owing to their structural integrity and electrochemical stability. Lin *et al*. [7,8] developed lithium-ion batteries employing niobium-based bimetallic oxides (*e.g.* $CrNb_{11}O_{29}$ and $Mg_2Nb_{34}O_{87}$) as anode materials, which store lithium via an intercalation mechanism (as confirmed by in-situ X-ray diffraction (XRD) spectroscopy), resulting in reversible electron transfer numbers of 23 and 68 moles, corresponding to high theoretical specific capacities of 401 and 396 mA h g^{-1}, respectively. Similarly, $CrNb_{11}O_{29}$ and $Mg_2Nb_{34}O_{87}$, synthesized *via* a solvothermal method, exhibited reversible specific capacities of 343 and 338 mA h g^{-1} at 0.1 C, respectively, with capacity losses of only 8.9 % after 400 cycles and 6.9 % after 500 cycles at 10 C, respectively, demonstrating their high cycling stability. These results demonstrate the superior lithium-storage performance of niobium-based bimetallic oxides relative to their titanium-based counterparts, making them promising candidates for use as negative electrodes in LICs.

In this study, $CoNb_2O_6$ was synthesized by ionizing Nb_2O_5 in an alkaline solution and subsequent coprecipitation with Co ions. The obtained $CoNb_2O_6$ particles were anchored onto the abundant binding sites of graphene nanosheets, thereby enhancing dispersibility and minimizing aggregation. Additionally, the porous graphene structure buffers volume changes during charge-discharge cycles, inhibiting the release of bound active material and improving the structural integrity and cycling

stability of the anode. This approach offers an efficient strategy to improve the performance of electrode materials, thereby facilitating the practical development of energy-storage devices.

Experimental

All reagents were of analytical grade and used as received without further purification.

Synthesis of $CoNb_2O_6$@G

In a typical preparation, graphene oxide (GO) was synthesized from natural graphite *via* a modified Hummers method [9,10]. Subsequently, 0.2 g of Nb_2O_5 and 1.5 g of KOH were dissolved in 30 mL of deionized water with continuous agitation. The obtained mixture was then placed into a 50-mL Teflon-lined stainless steel autoclave and subjected to hydrothermal treatment at 220 °C for 24 h to convert Nb_2O_5 into $[Nb_6O_{19}]^{8-}$. After cooling in the air, the pH was adjusted to approximately 8 using HCl (1 mol L^{-1}). Separately, $CoCl_2$ (with a Co-to-Nb molar ratio of 1:2) and varying amounts of GO (0, 50, 100, and 200 mg) were dispersed in deionized water (50 mL) and gradually added to the $[Nb_6O_{19}]^{8-}$ solution under continuous stirring. This mixture was then transferred to a Teflon-lined autoclave (100 mL) and heated at 220 °C for 48 h. The resulting $CoNb_2O_6$@G-*x* (where *x* is the GO content) products were washed repeatedly with ethanol and deionized water, and thereafter calcined at 500 °C for 2 h in a 10 % H_2/90 % Ar atmosphere to achieve high crystallinity.

Preparation of electrode

The working electrode was fabricated by blending conductive carbon black, PVDF binder, and $CoNb_2O_6$@G active material at a mass ratio of 1:1:8. NMP solvent was introduced with constant agitation to yield a uniform slurry. This slurry was evenly cast onto a 75 µm thick Cu foil current collector, followed by vacuum drying at 60°C for 24 h. The resulting electrode sheet was subsequently punched into 14 mm diameter disks, with an active material areal loading of approximately 4 mg cm^{-2}. For the counter electrode, activated carbon was processed *via* an analogous method and applied to Al foil at an elevated loading of 22 mg cm^{-2} to guarantee sufficient capacity.

Characterization

The morphology and microstructure of $CoNb_2O_6$@G and $CoNb_2O_6$ were examined by scanning electron microscopy (SEM, JEOL JSM-6480, Japan) and transmission electron microscopy (TEM, FEI Tecnai G2S-Twin, USA; Philips, Netherlands). X-ray diffraction (XRD, Rigaku TTR III, Japan) employing Cu-Kα radiation (λ = 0.1514 nm) was utilized to determine the crystalline structure of the materials at a scanning rate of 5° min^{-1}. Vibrational properties of $CoNb_2O_6$@G and $CoNb_2O_6$ were investigated using Raman spectroscopy (Renishaw InVia Reflex, UK, 532 nm laser excitation). The bulk elemental composition was determined using a Vario Micro cube elemental analyzer (Elementar, Germany), and the surface chemical states were assessed using X-ray photoelectron spectroscopy (XPS; Thermo Fisher ESCALAB^{TM} 250Xi, USA).

Electrochemical measurements

The electrochemical performance of $CoNb_2O_6$@G was evaluated using CR2032-type two-electrode coin cells, where a lithium metal foil and AC served as the positive and negative electrodes, respectively. The specific capacity (C, F g^{-1}) of the LIC was calculated based on the discharge duration observed in the galvanostatic charge-discharge (GCD) profile, employing Equations (1) and (2) [11].

$$S = \int V(t)\mathrm{d}t \quad (1)$$

$$C = 2IS/m\Delta V^2 \quad (2)$$

where S / V s is the integral area under the discharge curve, I / A is the charge-discharge current, m / g is the total mass of the active material in both the anode and cathode, and ΔV / V is the working potential (excluding the IR drop).

Equations (3) and (4) were utilized to determine the energy density (E / Wh kg^{-1}) and power density (P / W kg^{-1}), respectively [12,13]:

$$E = C\Delta V^2/7.2 \quad (3)$$

$$P = 3600E / \Delta t \quad (4)$$

where Δt / s is the discharge time.

Results and discussion

Figure 1a shows the XRD patterns of G, $CoNb_2O_6$, and their composite ($CoNb_2O_6$@G-100mg). The diffraction pattern of G displays a broad (002) peak at 24.95°, characteristic of graphitic carbon [14,15].

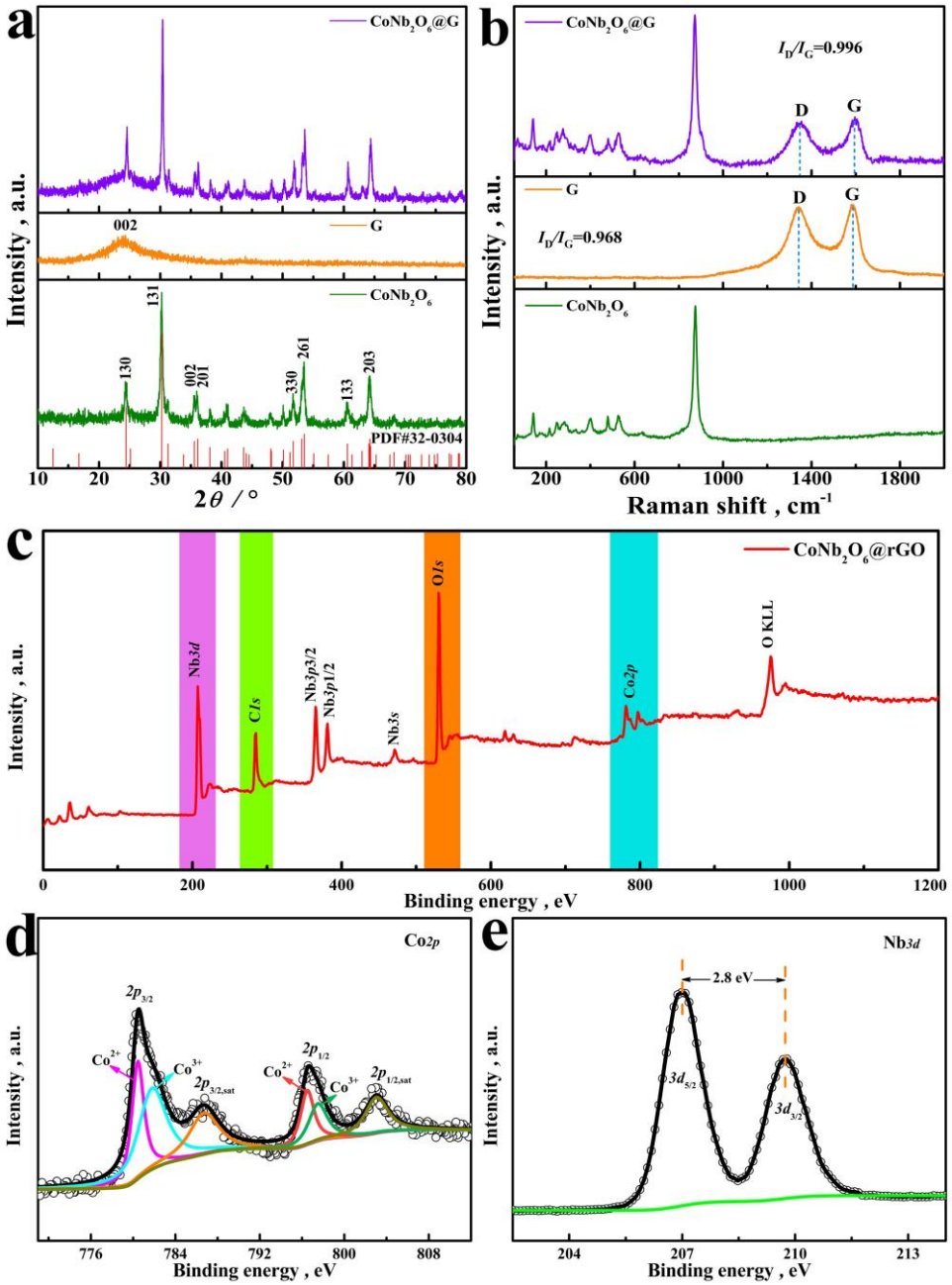

Figure 1. *(a) XRD patterns and (b) Raman spectra of G, $CoNb_2O_6$, and $CoNb_2O_6$@G-100mg; (c) XPS survey spectra of $CoNb_2O_6$@G-100mg; and high-resolution (d) Co 2p and (e) Nb 3d core-level XPS profiles of $CoNb_2O_6$@G-100mg*

All reflections observed in the pattern of pristine $CoNb_2O_6$ are indexed to an orthorhombic phase (JCPDS No. 32-0304), with prominent peaks at 24.4, 30.3, 35.5, 36.1, 51.7, 53.5, 60.6 and 64.2° corresponding to the (130), (131), (002), (201), (330), (261), (133) and (203) planes, respectively [16,17]. All peaks characteristic of G and $CoNb_2O_6$ appear in the XRD pattern of the $CoNb_2O_6$@G-100mg composite, confirming its phase purity, high crystallinity, and the absence of detectable impurities.

The structural features of $CoNb_2O_6$@G were characterized by Raman spectroscopy (Figure 1b). The spectra of the composites reveal two characteristic bands at 1350 cm^{-1} (D band) and 1582 cm^{-1} (G band), ascribed to the disorder-related breathing modes and in-plane stretching vibrations of sp^2-hybridized carbon in graphite, respectively [18,19]. The intensity ratio (I_D/I_G) derived from the spectrum of $CoNb_2O_6$@G (0.996) is higher than that derived from the spectrum of G (0.968), suggesting that the incorporation of $CoNb_2O_6$ introduces additional structural defects into the graphene framework that increase the surface area and enrich defect sites, thereby promoting Li^+ ion adsorption and charge-storage kinetics, which are advantageous for electrochemical applications [20,21].

The Raman spectrum of $CoNb_2O_6$ exhibits characteristic vibrational modes consistent with a columbite-type crystal structure. The low-frequency region (<300 cm^{-1}) is dominated by bending vibrations involving multiple oxygen coordination environments. Specifically, the v_{11} (B_{3g}) mode at 141.2 cm^{-1} is attributed to coupled O_c-Nb-O_t and O_b-Nb-O_b bending vibrations, whereas the v_9 (A_g) mode at 218.6 cm^{-1} arises from a combination of O-Co-O bending and O-Nb-O deformations. Two A_g modes (v_8 and v_7) indicative of strong coupling between Co-O stretching and O-Nb-O bending vibrations dominate the intermediate frequency range (249.4 to 276.2 cm^{-1}), highlighting the interconnected octahedral framework. In the high-frequency region, the v_5 (A_g) and v_4 (B_{1g}) modes at 397.8 and 480.3 cm^{-1}, respectively, are assigned to Nb-O_c stretching vibrations with superimposed O-Nb-O bending distortions. The v_3 (A_g) mode at 528.8 cm^{-1} corresponds to Nb-O_b stretching, a characteristic of bridging oxygen. The most intense Raman peak at 872.6 cm^{-1} (v_1 (A_g)) is attributed to the symmetric stretching of Nb-O_t bonds, consistent with terminal oxygen atoms in the columbite structure [22-24].

The chemical states of $CoNb_2O_6$@G-100mg were determined using XPS. The XPS survey spectrum (Figure 1c) exhibits peaks corresponding to Nb, Co, O, and C elements. Peaks at 803.04 and 786.85 eV in the high-resolution Co 2p spectrum (Figure 1d) are the satellite peaks (denoted "Sat") of the Co $2p_{1/2}$ and Co $2p_{3/2}$ signals, respectively. The main Co $2p_{1/2}$ and Co $2p_{3/2}$ peaks were deconvoluted into the following four components: two attributed to Co^{2+} at 780.5 and 796.5 eV, and two attributed to Co^{3+} at 781.8 and 797.3 eV. The formation of Co^{3+} resulted from the oxidation of the material in air [25,26]. The XPS spectrum of Nb 3d (Figure 1e) displays peaks corresponding to Nb $3d_{5/2}$ and Nb $3d_{3/2}$ at binding energies of 207.1 eV and 209.9 eV, respectively, exhibiting a spin-orbit splitting of 2.8 eV. These positions match the expected core-level energies for Nb^{5+} [27,28]. Moreover, the high-resolution O 1s spectrum (Figure S1a, Supplementary material) was fitted with four components attributed to C=O, C-O, O-H, and $CoNb_2O_6$ at 532.6, 531.7, 530.7 and 530.15 eV, respectively [29]. Fitting of the C 1s spectrum (Figure S1b) yields four peaks at 284.6, 285.5, 286.5 and 288.8 eV, assigned to C-C, C=C, C=O, and COOH functional groups, respectively [30].

The N_2 adsorption-desorption isotherms of the $CoNb_2O_6$@G composites are shown in Figure S2a. All samples exhibit type IV isotherms with H3/H4 hysteresis loops according to the IUPAC classification, suggesting the presence of slit-shaped pores commonly found in graphene-based composites. The composite with 100 mg of graphene achieves the highest N_2 uptake of 280 cm^3 g^{-1} at a relative pressure of approximately 1.0, indicating an increased total pore volume and specific surface area. This enhancement is attributed to the effective inhibition of graphene restacking by

the $CoNb_2O_6$ nanoparticles, leading to the formation of a new interlayer structure. The corresponding BJH pore size distribution (Figure S2b) shows a prominent peak in the mesoporous range (2 to 50 nm), with minor contributions from micropores (<2 nm) and macropores (>50 nm). As the graphene content increases, the pore size distribution shifts toward larger mesopores. These improvements underscore the synergistic role of graphene in dispersing nanoparticles, mitigating agglomeration, and promoting the formation of accessible pores, potentially leading to enhanced electrochemical performance.

The influence of graphene content on the microstructure is elucidated based on the SEM images of $CoNb_2O_6$@G-*x* (Figure S3). From Figure 2a, it can be observed that $CoNb_2O_6$@G develops a distinct porous architecture composed of interconnected graphene sheets as the graphene content increases. This three-dimensional network provides abundant binding sites for $CoNb_2O_6$ nanoparticles, effectively suppressing their agglomeration, and enhances contact between the electrode and electrolyte, thus facilitating ion transport. The homogeneous distribution of $CoNb_2O_6$ on the graphene sheets was verified by energy-dispersive X-ray spectroscopy (EDS) elemental mapping (Figure 2b), which reveals uniform spatial distributions of C, Nb, and Co throughout the $CoNb_2O_6$@G-100mg composite.

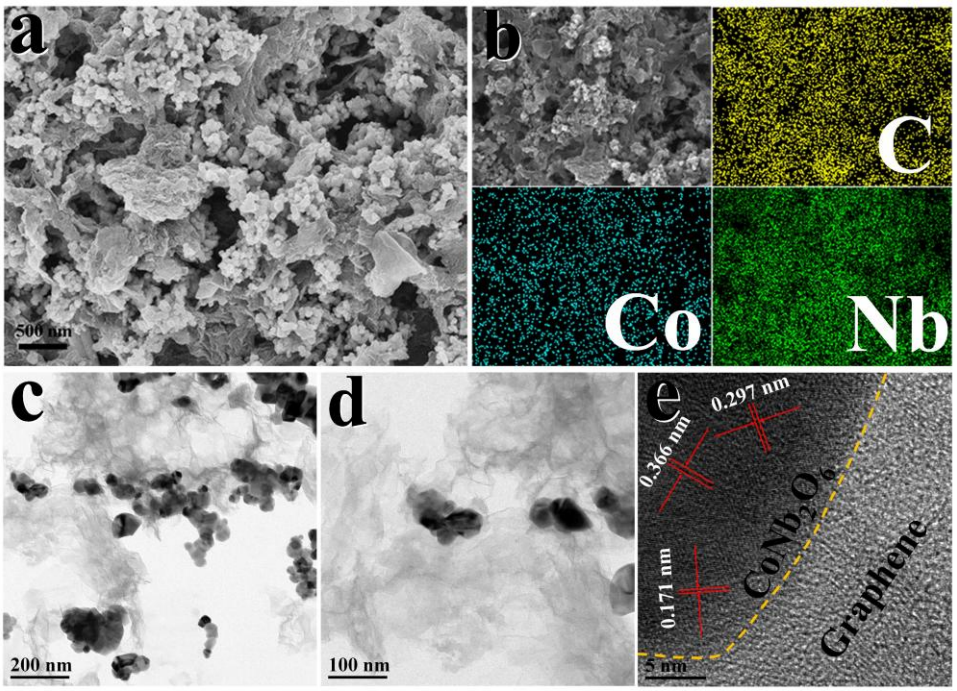

Figure 2. *(a) SEM image; (b) elemental mapping; (c, d) TEM images; and (e) HR-TEM image of $CoNb_2O_6$@G-100mg*

TEM images (Figures 2c and d) demonstrate robust adhesion between the $CoNb_2O_6$ nanoparticles and the graphene matrix, which is critical to maintain structural integrity during prolonged cycling. The disordered carbon layers of graphene alongside the well-defined lattice fringes of crystalline $CoNb_2O_6$ are shown in the corresponding high-resolution TEM (HR-TEM) image (Figure 2e). The measured *d*-spacing of the lattice fringes, corresponding to the (261), (131) and (130) planes of $CoNb_2O_6$, are 0.171, 0.297 and 0.366 nm, respectively, which is consistent with the XRD analysis and confirms the presence of the orthorhombic phase of $CoNb_2O_6$.

Figure 3 compares the electrochemical performances of the $CoNb_2O_6$@G-*x* composites. At a scan rate of 0.4 mV s^{-1}, the cyclic voltammetry (CV) curve of $CoNb_2O_6$@G-100mg (Figure 3a) exhibits the largest enclosed area, among those of the four composites, demonstrating its superior charge-

storage capability. Notably, the peak potential separation (Δ*V*) between the cathodic and anodic peaks systematically decreases with increasing graphene content, reflecting reduced polarization owing to the improved conductivity induced by graphene doping. Figure 3b presents the rate capability of the $CoNb_2O_6$@G-x composites under current densities varying between 50 and 2000 mA g^{-1}. At a current density of 50 mA g^{-1}, the composites with *x* = 0, 50, 100 and 200 exhibit capacities of 428.2, 473.7, 508.5 and 397.3 mA h g^{-1}, respectively. At a higher current density of 2000 mA g^{-1}, these capacities are reduced to 73.3, 159.8, 200.3 and 139.8 mA h g^{-1}, respectively. Upon returning to 50 mA g^{-1}, $CoNb_2O_6$@G-100mg outperforms the other composites, demonstrating the highest capacity retention of 90 %.

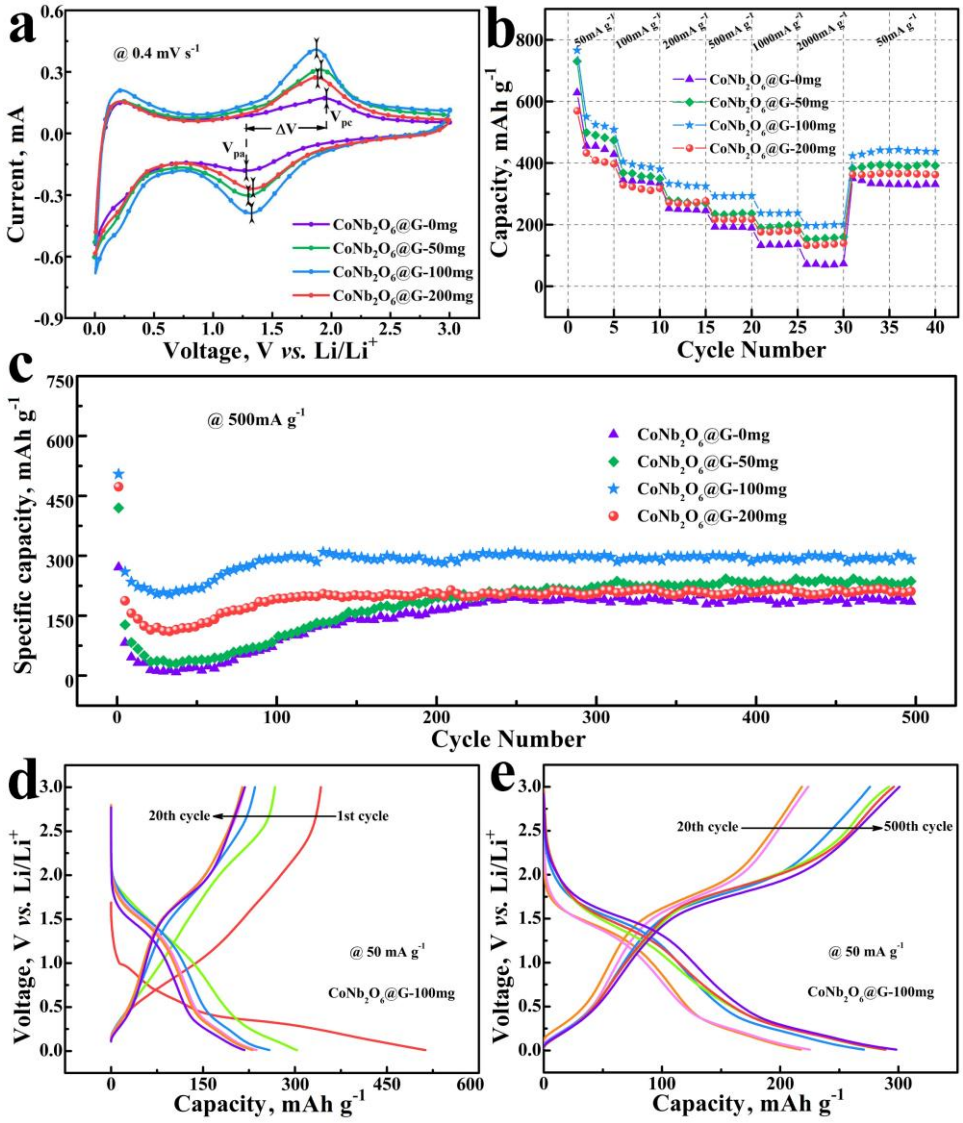

Figure 3. *Electrochemical performance of $CoNb_2O_6$@G-x: (a) CV curves at scan rate of 0.4 mV s^{-1}; (b) rate performance at current densities from 50 to 2000 mA g^{-1}; (c) long-term cycle life at a current density of 500 mA g^{-1}; and (d,e) charge-discharge curves during different cycles at a current density of 500 mA g^{-1}*

The long-term cycling stability of the $CoNb_2O_6$@G-*x* composite (Figure 3c), in combination with the corresponding charge-discharge curves (Figures 3d and 3e), shows that the capacity of the composite initially decreases, then increases before eventually stabilizing. This behavior is attributed to the formation of a solid-electrolyte interphase and the irreversible reaction of Li^+ with functional groups (-OH, *etc.*) on the surface of graphene. The fully activated $CoNb_2O_6$@G-*x*

composites exhibit minimal capacity fading over 500 cycles, demonstrating excellent cycling stability. In particularly, $CoNb_2O_6$@G-100mg demonstrates the highest capacity, primarily owing to the abundance of active sites afforded by graphene, and prevents the agglomeration of $CoNb_2O_6$. However, excessive graphene doping can reduce the capacity of the composite owing to the relatively low Li^+ storage capacity of graphene.

The reaction kinetics of $CoNb_2O_6$@G-100mg were further analyzed by CV. The CV curve of the sample (Figure 4a) shows a pair of redox peaks at 1.25 and 1.75 V, corresponding to a reversible electrochemical reaction involving the Nb^{4+}/Nb^{5+} and Nb^{3+}/Nb^{4+} redox couples. This reaction leads to the intercalation and deintercalation of Li^+ (Equation (5)) [31,32]:

$$CoNb_2O_6 + nLi^+ + ne^- = Li_nCoNb_2O_6\ (0 \le n \le 4) \quad (5)$$

Here, n denotes the mole fraction of the intercalated Li^+. Additionally, the high rate performance is elucidated based on an analysis of the redox pseudocapacitance contribution of the $CoNb_2O_6$@G--100 mg electrode.

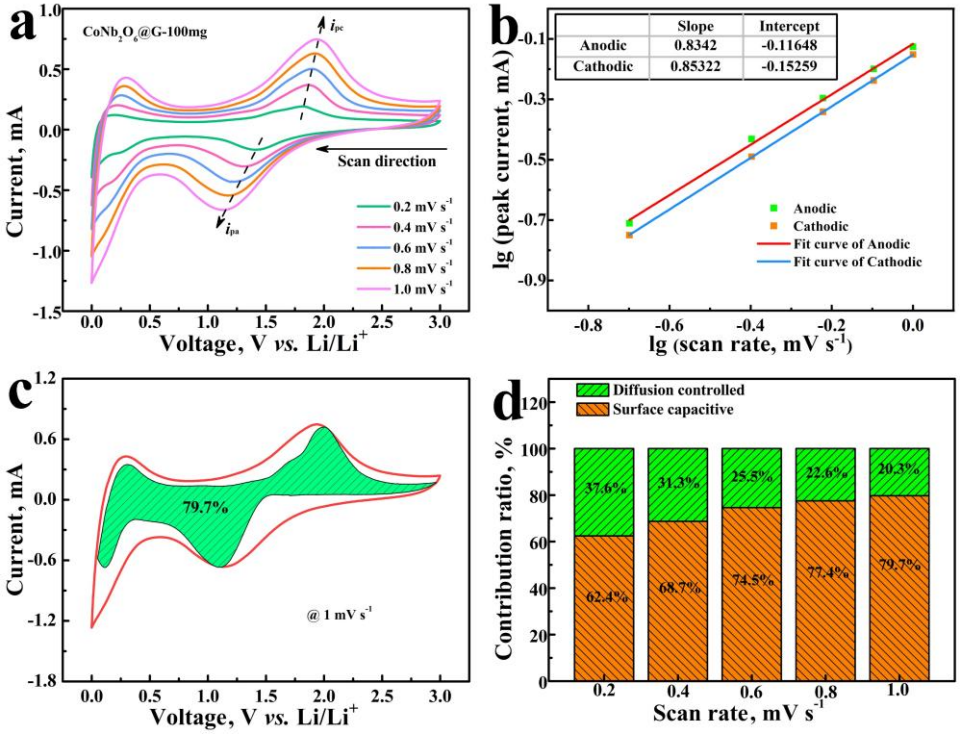

Figure 4. *(a) CV curves of $CoNb_2O_6$@G-100mg at various scan rates from 0.2 to 1.0 mV s^{-1}; (b) relationship between lg i_p and lg v; (c) separation of the capacitive and diffusion-controlled currents in $CoNb_2O_6$@G-100mg at a scan rate of 1 mV s^{-1}; and (d) ratio of the capacitive- and diffusion-controlled charge at various scan rates*

Equation (6) typically characterizes the dependence of the response current (i) on the scan rate (ν) [33,34]:

$$i = a\nu^b\ (0.5 \le b \le 1) \quad (6)$$

where a and b are adjustable parameters. Applying a logarithmic operation to Equation (5) gives Equation (7):

$$\lg i = b \lg \nu + \lg a\ (0.5 \le b \le 1) \quad (7)$$

The b parameter is derived from the gradient of the log i versus log ν plot, functioning as a descriptor of the dominant charge storage process. Higher b values indicate a greater similarity between the operating charge-storage mechanism and an ideal capacitive process. The b values of $CoNb_2O_6$@G-100mg are approximately 0.83 and 0.85 at the reduction and oxidation peaks, respectively (Figure 4b),

which implies that the charge-storage process is primarily governed by a capacitive mechanism, with a diffusion-controlled mechanism playing a minor role. In particular, the capacitive and diffusion-controlled charge-storage processes can be further quantified using Equation (8) [35,36]:

$$i(V) = k_1 \nu + k_2 \nu^{1/2} \quad (8)$$

At a fixed potential V, the observed current i arises from the combination of capacitive contribution ($k_1\nu$) and diffusion-controlled component ($k_2 \nu^{1/2}$). The proportions of capacitive and diffusion-limited mechanisms were evaluated through cyclic voltammetry (CV) conducted at a scan rate of 1 mV s^{-1} (Figure 4c). The capacitive mechanism constitutes 79.7 % of the overall capacity, suggesting efficient capacitive kinetics in $CoNb_2O_6$@G-100mg that give rise to its superior rate capability. Similarly, at scan rates of 0.2, 0.4, 0.6 and 0.8 mV s^{-1}, the capacitive effect accounts for 62.7, 68.7, 74.5 and 77.4 % of the total capacity, respectively.

Based on the excellent Li storage capacity of the $CoNb_2O_6$@G-100mg electrode, an LIC was assembled using $CoNb_2O_6$@G-100mg and AC as the anode and cathode, respectively, using a 1 M $LiPF_6$ electrolyte in a mixture of ethylene carbonate and diethyl carbonate (1:1, v/v) to evaluate its feasibility. The electrochemical performance of the AC electrode in the half-cell is shown in Figure S4. The optimal mass ratio of $CoNb_2O_6$@G-100mg to AC is 1:6, as determined by Equation (9) [37,38]:

$$m^-/m^+ = C^+\Delta V^+ / C^-\Delta V^- \quad (9)$$

Figure 5a shows the CV curves of the assembled $CoNb_2O_6$@G-100mg//AC LIC in different operating voltage windows. The response current remains stable between 0.0 and 3.5 V, indicating the absence of electrolyte decomposition within this voltage range. The CV curves at various scan rates (Figure 5b) exhibit a quasi-rectangular shape attributed to the distinct reaction kinetics of the anode and cathode.

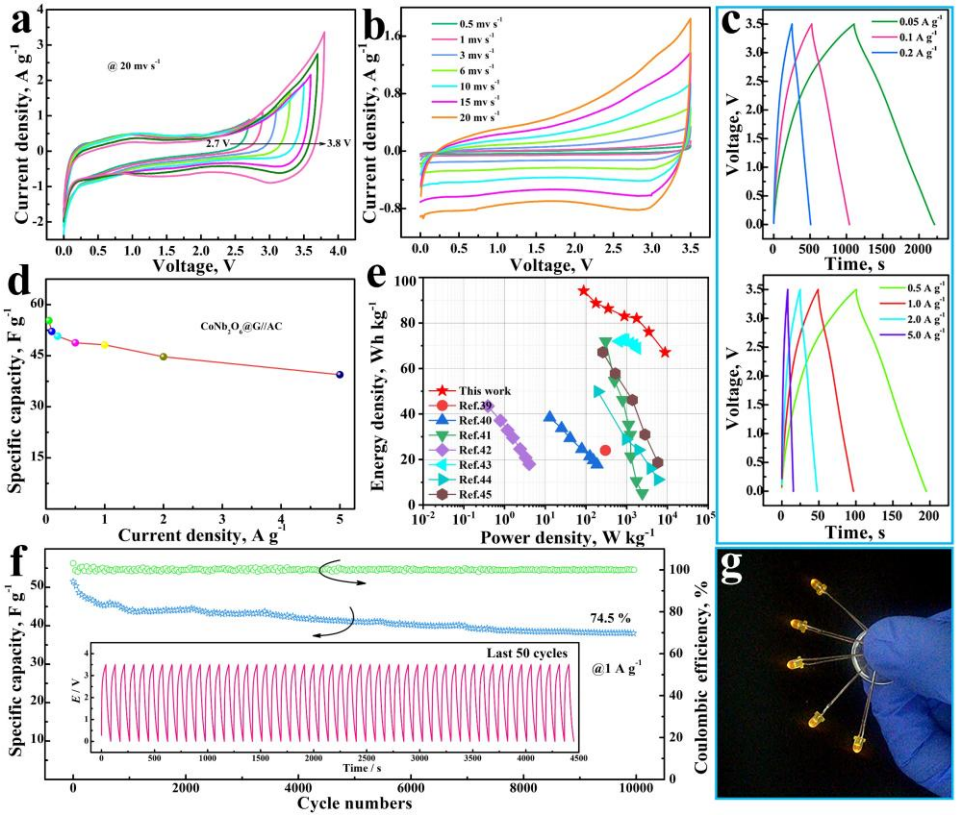

Figure 5. *Electrochemical properties of $CoNb_2O_6$@G-100mg//AC LIC: (a) CV curves in voltage window from 0.0 to 3.8 V; (b) CV scans at rates of 0.5 to 20 mV s^{-1}; (c) GCD curves at densities of 0.05 to 5.0 A g^{-1}; (d) specific capacitance vs. current density; (e) Ragone plots; (f) Cycling stability and Coulombic efficiency at 1 A g^{-1}; (g) Photo of LEDs powered by $CoNb_2O_6$@G-100mg//AC LIC*

As the scan rate increased, the current response correspondingly enhanced, with minimal distortion in the CV profile even at an elevated rate of 20 mV s^{-1}, highlighting the device's robust stability during Li^+ insertion/extraction processes. The GCD profiles of the devices display a nonlinear triangular form across different current densities, which is attributable to the distinct charge-storage behaviors of the intercalation-type cathode and the electric double-layer anode. The discharge profile exhibits a limited voltage drop, signifying superior electrode conductivity that minimizes the device's internal resistance. The device's specific capacitance, calculated *via* Equation (2), is illustrated in Figure 5d. For the $CoNb_2O_6$@G//AC LIC, the specific capacitances at current densities of 0.05, 0.1, 0.2, 0.5, 1, 2 and 5 A g^{-1} were measured as 55.3, 52.1, 50.7, 48.8, 48.2, 44.7 and 39.4 F g^{-1}, respectively. The modest capacitance decay observed at higher current densities underscores the device's outstanding rate capability.

Figure 5e presents the Ragone plot, illustrating the trade-off between power and energy densities. It reveals that the CoNb2O6@G-100mg//AC lithium-ion capacitor achieves a peak energy density of 94.1 Wh kg-1 at a power density of 87.5 W kg^{-1}, alongside a maximum power density of 8750 W kg^{-1} at an energy density of 67.1 Wh kg^{-1}. These performance metrics outperform those reported for comparable metal-oxide-based LICs (Table 1) [39-45]. The evaluation of the cyclic performance of the $CoNb_2O_6$@G-100mg//AC LIC is shown in Figure 5f. At a current density of 1 A g^{-1}, the device exhibits a capacity retention of 74.5 % after 10,000 charge-discharge cycles, with a cycle-to-cycle capacitance loss of only 0.00255 %, demonstrating excellent cycling stability. The $CoNb_2O_6$@G-100mg//AC LIC was directly connected to five yellow light-emitting diodes (LEDs) to further assess its practical applicability. All five LEDs were powered and continuously illuminated for 10 min (Figure 5g).

Table 1. *Comparison of the electrochemical performance of the $CoNb_2O_6$@G//AC LIC with those of some existing LICs*

Anode//cathode	Voltage range, V	Cycling stability, % (Cycling number)	Maximum energy density, W h kg^{-1}	Maximum power density, W kg^{-1}	Ref.
$CuBi_2O_4$//AC	0.0 to 3.0	86 (1500)	24	300	[39]
$LiMn_2O_4$/graphene//AC	0.0 to 2.3	90.6 (500)	38.8	186.5	[40]
TiO_2@graphene//graphene	0.0 to 3.0	68 (1000)	72	2000	[41]
$TiNb_2O_7$//AC	1.0 to 3.0	84 (3000)	43	3000	[42]
$Li_4Ti_5O_{12}$/C//PGM	1.0 to 3.0	65 (1000)	40	8300	[43]
$H_2Ti_{11.85}Nb_{0.15}O_{25}$//AC	\	84 (10000)	24.3	5821	[44]
Ti_3C_2Tx/CNT//AC	1.0 to 4.0	81.3 (5000)	67	5797	[45]
$CoNb_2O_6$@G-100mg//AC LIC	0.0 to 3.5	74.5 (10000)	94.1	8750	Our work

Conclusions

$CoNb_2O_6$@G was prepared *via* a two-step hydrothermal method, and its lithium-storage performance was further optimized by adjusting the graphene content. The particle size of $CoNb_2O_6$ ranged from 50 to 60 nm. With a graphene content of 100 mg, $CoNb_2O_6$@G-100mg exhibited the highest specific capacity of 508.5 mA h g^{-1} at a current density of 50 mA g^{-1} along with an outstanding rate capability. Additionally, a hybrid LIC, with an anode and cathode consisting of $CoNb_2O_6$@G-100mg and AC, respectively, achieved maximum energy and power densities of 94.1 W h kg^{-1} and 8750 W kg^{-1}, respectively, in the operating voltage range of 0.0 to 3.5 V, along with a capacity loss of only 25.5 % after 10,000 cycles, demonstrating excellent cycling performance. The $CoNb_2O_6$@G anode holds significant potential applications in LICs with high energy, fast charging, and high stability. Furthermore, our findings offer valuable insights that will inform the design of next-generation high-performance energy storage devices.

Acknowledgements: *Not applicable.*

Funding: *This work was supported by the Natural Science Foundation of Ningxia (No. 2022AAC05033); the Fundamental Research Funds of the Central Universities, North Minzu University (Nos. 2020KYQD18 and 2021KJCX04); the Key Research and Development Program (Talents Introduction Project) of Ningxia (No. 2021BEB04027); National Natural Science Foundation of China (No. U22A20146); and Ningxia Science & Technology Innovation Team of High-Performance Secondary Battery Key Materials and Devices (No. 2024CXTD003).*

References

[1] J. Han, A. Hirata, J. Du, Y. Ito, T. Fujita, S. Kohara, T. Ina, M. Chen, Intercalation pseudocapacitance of amorphous titanium dioxide@nanoporous graphene for high-rate and large-capacity energy storage, *Nano Energy* **49** (2018) 354-362. https://doi.org/10.1016/j.nanoen.2018.04.063

[2] J. Ding, H. Wang, Z. Li, K. Cui, D. Karpuzov, X. Tan, A. Kohandehghan, D. Mitlin, Peanut shell hybrid sodium ion capacitor with extreme energy-power rivals lithium ion capacitors, *Energy & Environmental Science* **8** (2015) 941-955. https://doi.org/10.1039/c4ee02986k

[3] J. Wang, X. Zhang, Q. Wei, H. Lv, Y. Tian, Z. Tong, X. Liu, J. Hao, H. Qu, J. Zhao, Y. Li, L. Mai, 3D self-supported nanopine forest-like Co_3O_4@$CoMoO_4$ core-shell architectures for high-energy solid state supercapacitors, *Nano Energy* **19** (2016) 222-233. https://doi.org/10.1016/j.nanoen.2015.10.036

[4] Z. N. Ezhyeh, M. Khodaei, F. Torabi, Review on doping strategy in $Li_4Ti_5O_{12}$ as an anode material for Lithium-ion batteries, *Ceramics International* **49** (2023) 7105-7141. https://doi.org/10.1016/j.ceramint.2022.04.340

[5] Q. Pan, S. Zhang, B. Chen, S. Sun, F. Han, G. Meng, Fe_2O_3 nanoparticles encapsulated in the inner walls of integrated 3D carbon tube grid as high-performance anode for lithium-ion batteries, *Journal of Power Sources* **602** (2024) 234348. https://doi.org/10.1016/j.jpowsour.2024.234348

[6] S. Ahn, Y. Nakamura, H. Nara, T. Momma, W. Sugimoto, T. Osaka, Application of Sn-Ni Alloy as an Anode for Lithium-Ion Capacitors with Improved Volumetric Energy and Power Density, *Journal of The Electrochemical Society* **166** (2019) A3615. https://doi.org/10.1149/2.0661915jes

[7] Q. Fu, X. Liu, J. Hou, Y. Pu, C. Lin, L. Yang, X. Zhu, L. Hu, S. Lin, L. Luo, Y. Chen, Highly conductive $CrNb_{11}O_{29}$ nanorods for use in high-energy, safe, fast-charging and stable lithium-ion batteries, *Journal of Power Sources* **397** (2018) 231-239. https://doi.org/10.1016/j.jpowsour.2018.07.020

[8] X. Zhu, Q. Fu, L. Tang, C. Lin, J. Xu, G. Liang, R. Li, L. Luo, Y. Chen, $Mg_2Nb_{34}O_{87}$ Porous Microspheres for Use in High-Energy, Safe, Fast-Charging, and Stable Lithium-Ion Batteries, *ACS Applied Materials & Interfaces* **10** (2018) 23711-23720. https://doi.org/10.1021/acsami.8b03997

[9] Z. Yang, M. Zhang, Y. Liu, M. Jiang, Y. Sun, J. Wang, J. Xu, J. Liu, Composite of $CoS_{1.97}$ nanoparticles decorated CuS hollow cubes with rGO as thin film electrode for high-performance all solid flexible supercapacitors, *Journal of Colloid and Interface Science* **664** (2024) 691-703. https://doi.org/10.1016/j.jcis.2024.03.083

[10] R. M. Bhattarai, K. Chhetri, N. Le, D. Acharya, S. Saud, M. C. H. P. L. Nguyen, S. J. Kim, Y. S. Mok, Oxygen functionalization-assisted anionic exchange toward unique construction of flower-like transition metal chalcogenide embedded carbon fabric for ultra-long life flexible energy storage and conversion, *Carbon Energy* **6** (2023) e392. https://doi.org/10.1002/cey2.392

[11] A. C. Mendhe, A. Kore, S. D. Dhas, Y. Kim, R. Batool, A. Ghazal, D. Kim, High-performance supercapacitor electrodes: Hierarchical integration of bimetallic structures incorporating silver and copper phosphates with a 3D fernlike stellar dendritic architecture, *Chemical Engineering Journal* **489** (2024) 151168. https://doi.org/10.1016/j.cej.2024.151168

[12] K. Li, X. Wang, S. Li, P. Urbankowski, J. Li, Y. Xu, Y. Gogotsi, An Ultrafast Conducting Polymer@MXene Positive Electrode with High Volumetric Capacitance for Advanced Asymmetric Supercapacitors, *Small* **16** (2020) e1906851. https://doi.org/10.1002/smll.201906851

[13] M. Kong, Y. Liu, B. Zhou, K. Yang, J. Tang, P. Zhang, W. H. Zhang, Rational Design of Sb@C@TiO_2 Triple-Shell Nanoboxes for High-Performance Sodium-Ion Batteries, *Small* 16 (2020) e2001976. https://doi.org/10.1002/smll.202001976.

[14] M. Wang, Z. Yang, W. Li, L. Gu, Y. Yu, Superior Sodium Storage in 3D Interconnected Nitrogen and Oxygen Dual-Doped Carbon Network, *Small* **12** (2016) 2559-2566. https://doi.org/10.1002/smll.201600101

[15] D. Hu, Y. Jia, S. Yang, C. Lin, F. Huang, R. Wu, S. Guo, K. Xie, P. Du, Hierarchical nanocomposites of redox covalent organic frameworks nanowires anchored on graphene sheets for super stability supercapacitor, *Chemical Engineering Journal* **488** (2024) 151160. https://doi.org/10.1016/j.cej.2024.151160

[16] J. Liang, J. Xing, S. Guan, B. Zhang, X. Fu, Hierarchical $CoNb_2O_6$@CoOOH core-shell composite on carbon fabric for aqueous supercapacitor anode with high capacitance and super-long life, *Electrochimica Acta* **406** (2022) 139845. https://doi.org/10.1016/j.electacta.2022.139845

[17] R. Ma, F. Cao, J. Wang, G. Zhu, G. Pang, Hydrothermal synthesis and phase stability of $CoNb_2O_6$ with a rutile structure, *Materials Letters* **65** (2011) 2880-2882. https://doi.org/10.1016/j.matlet.2011.06.084

[18] Y. Xue, X. Guo, M. Wu, J. Chen, M. Duan, J. Shi, J. Zhang, F. Cao, Y. Liu, Q. Kong, Zephyranthes-like Co_2NiSe_4 arrays grown on 3D porous carbon frame-work as electrodes for advanced supercapacitors and sodium-ion batteries, *Nano Research* **14** (2021) 3598-3607. https://doi.org/10.1007/s12274-021-3640-4

[19] Y. Luo, W. Que, Y. Tang, Y. Kang, X. Bin, Z. Wu, B. Yuliarto, B. Gao, J. Henzie, Y. Yamauchi, Regulating Functional Groups Enhances the Performance of Flexible Microporous MXene/Bacterial Cellulose Electrodes in Supercapacitors, *ACS Nano* **18** (2024) 11675-11687. https://doi.org/10.1021/acsnano.3c11547

[20] Y. Wang, S. Chou, D. Wexler, H. Liu, S. Dou, High-Performance Sodium-Ion Batteries and Sodium-Ion Pseudocapacitors Based on MoS_2/Graphene Composites, *Chemistry - A European Journal* **20** (2014) 9607-9612. https://doi.org/10.1002/chem.201402563

[21] Z. Zhang, Y. Fu, X. Yang, Y. Qu, Z. Zhang, Hierarchical $MoSe_2$ Nanosheets/Reduced Graphene Oxide Composites as Anodes for Lithium-Ion and Sodium-Ion Batteries with Enhanced Electrochemical Performance, *Chemnanomat* **1** (2015) 409-414. https://doi.org/10.1002/cnma.201500097

[22] F. Huang, Q. Zhou, L. Li, X. Huang, D. Xu, F. Li, T. Cui, Structural Transition of $MnNb_2O_6$ under Quasi-Hydrostatic Pressure, *The Journal of Physical Chemistry C* **118** (2014) 19280-19286. https://doi.org/10.1021/jp503542y

[23] D. L. Rousseau, R. P. Bauman, S. P. S. Porto, Normal mode determination in crystals, *Journal of Raman Spectroscopy* **10** (1981) 253-290. https://doi.org/10.1002/jrs.1250100152

[24] E. Husson, Y. Repelin, N. Q. Dao, H. Brusset, Normal coordinate analysis for $CaNb_2O_6$ of columbite structure, *The Journal of Chemical Physics* **66** (1977) 5173-5180. https://doi.org/10.1063/1.433780

[25] J. Wang, Y. Huang, X. Du, S. Zhang, M. Zong, Hollow 1D carbon tube core anchored in Co_3O_4@SnS_2 multiple shells for constructing binder-free electrodes of flexible supercapacitors, *Chemical Engineering Journal* **464** (2023) 142741. https://doi.org/10.1016/j.cej.2023.142741

[26] M. Zhang, H. Fan, N. Zhao, H. Peng, X. Ren, W. Wang, H. Li, G. Chen, Y. Zhu, X. Jiang, P. Wu, 3D hierarchical $CoWO_4$/Co_3O_4 nanowire arrays for asymmetric supercapacitors with high energy density, *Chemical Engineering Journal* **347** (2018) 291-300. https://doi.org/10.1016/j.cej.2018.04.113

[27] T. Wang, T. Ma, T. Ge, S. Shi, H. Ji, W. Li, G. Yang, Synthesis of $MnNb_2O_6$ with hierarchical structure as a novel electrode material for high-performance supercapacitors, *Journal of Alloys and Compounds* **750** (2018) 428-435. https://doi.org/10.1016/j.jallcom.2018.04.031

[28] J. Wu, J. Wang, H. Li, Y. Li, Y. Du, Y. Yang, X. Jia, Surface activation of $MnNb_2O_6$ nanosheets by oxalic acid for enhanced photocatalysis, *Applied Surface Science* **403** (2017) 314-325. https://doi.org/10.1016/j.apsusc.2017.01.170

[29] A. Lakshmi-Narayana, N. Attarzadeh, V. Shutthanandan, C. V. Ramana, High-Performance $NiCo_2O_4$/Graphene Quantum Dots for Asymmetric and Symmetric Supercapacitors with Enhanced Energy Efficiency, *Advanced Functional Materials* **34** (2024) 2316379. https://doi.org/10.1002/adfm.202316379

[30] C. Zhang, Y. Xu, G. Du, Y. Wu, Y. Li, H. Zhao, U. Kaiser, Y. Lei, Oxygen-functionalized soft carbon nanofibers as high-performance cathode of K-ion hybrid capacitor, *Nano Energy* **72** (2020) 104661. https://doi.org/10.1016/j.nanoen.2020.104661

[31] C. Yang, Y. Zhang, F. Lv, C. Lin, Y. Liu, K. Wang, J. Feng, X. Wang, Y. Chen, J. Li, S. Guo, Porous $ZrNb_{24}O_{62}$ nanowires with pseudocapacitive behavior achieve high-performance lithium-ion storage, *Journal of Materials Chemistry A* **5** (2017) 22297-22304. https://doi.org/10.1039/c7ta07347j

[32] T. Liu, P. Li, N. Yao, T. Kong, G. Cheng, S. Chen, W. Luo, Self-Sacrificial Template-Directed Vapor-Phase Growth of MOF Assemblies and Surface Vulcanization for Efficient Water Splitting, *Advanced Materials* **31** (2019) e1806672. https://doi.org/10.1002/adma.201806672

[33] Y. Wang, H. Tang, Q. Xie, J. Liu, S. Sun, M. Zhou, Y. Zhang, pH-Regulated host-guest architecture in molybdenum Dioxide/Carbon sphere composites for flexible solid-state supercapacitors, *Chemical Engineering Journal* **481** (2024) 148558. https://doi.org/10.1016/j.cej.2024.148558

[34] G. Wang, R. Zhang, H. Zhang, K. Cheng, Aqueous MXene inks for inkjet-printing microsupercapacitors with ultrahigh energy densities, *Journal of Colloid and Interface Science* **645** (2023) 359-370. https://doi.org/10.1016/j.jcis.2023.04.155

[35] Y. Long, X. An, H. Zhang, J. Yang, L. Liu, Z. Tian, G. Yang, Z. Cheng, H. Cao, H. Liu, Y. Ni, Highly graphitized lignin-derived porous carbon with hierarchical N/O co-doping “core-shell” superstructure supported by metal-organic frameworks for advanced supercapacitor performance, *Chemical Engineering Journal* **451** (2023) 138877. https://doi.org/10.1016/j.cej.2022.138877

[36] R. Chen, X. Cai, X. He, X. Hong, Y. Liu, J.-K. So, B. Wang, Y. Zhou, L. Cheng, Z. Shen, High mass-loading CoO@NiCo-LDH//FeNiS flexible supercapacitor with high energy density and fast kinetics, *Chemical Engineering Journal* **484** (2024) 149736. https://doi.org/10.1016/j.cej.2024.149736

[37] H. Zhang, X. Zhang, H. Li, Y. Gao, J. Yan, K. Zhu, K. Ye, K. Cheng, G. Wang, D. Cao, Copper niobate nanowires immobilized on reduced graphene oxide nanosheets as rate capability anode for lithium ion capacitor, *Journal of Colloid and Interface Science* **583** (2021) 652-660. https://doi.org/10.1016/j.jcis.2020.09.076

[38] J. Gao, Z. Zhuang, X. Zhou, H. Xu, X. Xu, W. Li, Reversible Mn^{2+}/Mn^{4+} and Mn^{4+}/Mn^{6+} double-electron redoxes in heterostructure $MnS_2/MnSe_2$@HCMs boost high energy storage for hybrid supercapacitors, *Chemical Engineering Journal* **485** (2024) 149520. https://doi.org/10.1016/j.cej.2024.149520

[39] S. Yuvaraj, K. Karthikeyan, D. Kalpana, Y. S. Lee, R. K. Selvan, Surfactant-free hydrothermal synthesis of hierarchically structured spherical $CuBi_2O_4$ as negative electrodes for Li-ion hybrid capacitors, *Journal of Colloid and Interface Science* **469** (2016) 47-56. https://doi.org/10.1016/j.jcis.2016.01.060.

[40] J. Li, X. Zhang, R. Peng, Y. Huang, L. Guo, Y. Qi, $LiMn_2O_4$/graphene composites as cathodes with enhanced electrochemical performance for lithium-ion capacitors, *RSC Advances* **6** (2016) 54866-54873. https://doi.org/10.1039/c6ra09103b

[41] F. Wang, C. Wang, Y. Zhao, Z. Liu, Z. Chang, L. Fu, Y. Zhu, Y. Wu, D. Zhao, A Quasi-Solid-State Li-Ion Capacitor Based on Porous TiO_2 Hollow Microspheres Wrapped with Graphene Nanosheets, *Small* **12** (2016) 6207-6213. https://doi.org/10.1002/smll.201602331

[42] V. Aravindan, J. Sundaramurthy, A. Jain, P. S. Kumar, W. C. Ling, S. Ramakrishna, M. P. Srinivasan, S. Madhavi, Unveiling $TiNb_2O_7$ as an insertion anode for lithium ion capacitors with high energy and power density, *ChemSusChem* **7** (2014) 1858-1863. https://doi.org/10.1002/cssc.201400157

[43] L. Ye, Q. Liang, Y. Lei, X. Yu, C. Han, W. Shen, Z. Huang, F. Kang, Q. Yang, A high performance Li-ion capacitor constructed with $Li_4Ti_5O_{12}$/C hybrid and porous graphene macroform, *Journal of Power Sources* **282** (2015) 174-178. https://doi.org/10.1016/j.jpowsour.2015.02.028

[44] J. H. Lee, H. K. Kim, E. Baek, M. Pecht, S. H. Lee, Y. H. Lee, Improved performance of cylindrical hybrid supercapacitor using activated carbon/niobium doped hydrogen titanate, *Journal of Power Sources* **301** (2016) 348-354. https://doi.org/10.1016/j.jpowsour.2015.09.113

[45] P. Yu, G. Cao, S. Yi, X. Zhang, C. Li, X. Sun, K. Wang, Y. Ma, Binder-free 2D titanium carbide (MXene)/carbon nanotube composites for high-performance lithium-ion capacitors, *Nanoscale* **10** (2018) 5906-5913. https://doi.org/10.1039/c8nr00380g